Pupil Fluctuations Track Fast Switching of Cortical States during Quiet Wakefulness

Jacob Reimer,[1,*] Emmanouil Froudarakis,[1] Cathryn R. Cadwell,[1] Dimitri Yatsenko,[1] George H. Denfield,[1] and Andreas S. Tolias[1,2,*]
[1]Department of Neuroscience, Baylor College of Medicine, Houston, TX 77030, USA
[2]Department of Computational and Applied Mathematics, Rice University, Houston, TX 77005, USA
*Correspondence: jreimer@cns.bcm.edu (J.R.), atolias@cns.bcm.edu (A.S.T.)
http://dx.doi.org/10.1016/j.neuron.2014.09.033

SUMMARY

Neural responses are modulated by brain state, which varies with arousal, attention, and behavior. In mice, running and whisking desynchronize the cortex and enhance sensory responses, but the quiescent periods between bouts of exploratory behaviors have not been well studied. We found that these periods of "quiet wakefulness" were characterized by state fluctuations on a timescale of 1–2 s. Small fluctuations in pupil diameter tracked these state transitions in multiple cortical areas. During dilation, the intracellular membrane potential was desynchronized, sensory responses were enhanced, and population activity was less correlated. In contrast, constriction was characterized by increased low-frequency oscillations and higher ensemble correlations. Specific subtypes of cortical interneurons were differentially activated during dilation and constriction, consistent with their participation in the observed state changes. Pupillometry has been used to index attention and mental effort in humans, but the intracellular dynamics and differences in population activity underlying this phenomenon were previously unknown.

INTRODUCTION

Responses to external stimuli are strongly modulated by the brain's internal dynamics, which are organized around characteristic states that vary with arousal, attention, and behavioral context (Harris and Thiele, 2011; Iriki et al., 1996; Kahneman, 1973; Lee and Dan, 2012). Across multiple species, more active states are associated with cortical desynchronization, a reduction in the amplitude of low-frequency oscillations measured in EEG, LFP, or intracellular recordings. For example, primate cortex is more desynchronized during attentive states (Gould et al., 2011; Grent-'t-Jong et al., 2011; Rohenkohl and Nobre, 2011) and in REM sleep compared to deeper sleep stages (Colten and Altevogt, 2006).

Nonprimate mammals also display a spectrum of cortical dynamics during waking periods, from more synchronized to more desynchronized states, and this internal variability modulates responses to external stimuli (Hei et al., 2014; Zhuang et al., 2014). Specifically, recent work in awake mice has revealed that the cortex is desynchronized during bouts of exploratory behavior, such as whisking (Crochet and Petersen, 2006; Poulet and Petersen, 2008) and running (Bennett et al., 2013; Niell and Stryker, 2010; Polack et al., 2013), compared to stationary periods. In mouse primary visual cortex (V1), this desynchronization is coupled with an enhancement of sensory responses (Fu et al., 2014; Froudarakis et al., 2014) and a reduction in detection thresholds (Bennett et al., 2013), and similar effects are seen in primary somatosensory cortex (area S1; Zagha et al., 2013).

Between bouts of activity, there are longer epochs of "quiet wakefulness," periods of behavioral quiescence that have not been well studied. While previous reports have emphasized the average increase in low-frequency synchronous activity during quiet wakefulness, we observed second-to-second state fluctuations during these periods in both V1 and S1. Fast state fluctuations during quiet wakefulness were closely tracked by changes in pupil diameter. During dilation, we found that the cortex was desynchronized and more responsive to external stimuli, compared to constriction, when low-frequency oscillations were enhanced and ensemble correlations were increased. (In this study we always use "dilation" and "constriction" to refer to active dilating and constricting, and not the state of being dilated or constricted.) Furthermore, vasoactive intestinal peptide-expressing (VIP+) GABAergic interneurons and somatostatin-expressing (SOM+) interneurons were differentially modulated during dilation and constriction. These interneuron subtypes have recently been shown to participate in a canonical local circuit essential for the enhancement of visual responses during running (Fu et al., 2014), and our results suggest that this mechanism may be recapitulated in the state fluctuations that occur during quiet wakefulness.

RESULTS

Exploratory Behaviors Are Accompanied by Cortical Desynchronization and Pupil Dilation

We performed whole-cell patch-clamp recordings of layer 2/3 cortical neurons in awake mice (n = 111 total neurons from 38 animals) while monitoring treadmill motion, whisking behavior, eye movements, and pupil diameter (Figures 1A and 1B). All analyses in Figures 1, 2, and 3 were of spontaneous recordings, in order to avoid any confounding effects of visual stimuli. Periods of running, whisking, and eye movements usually occurred
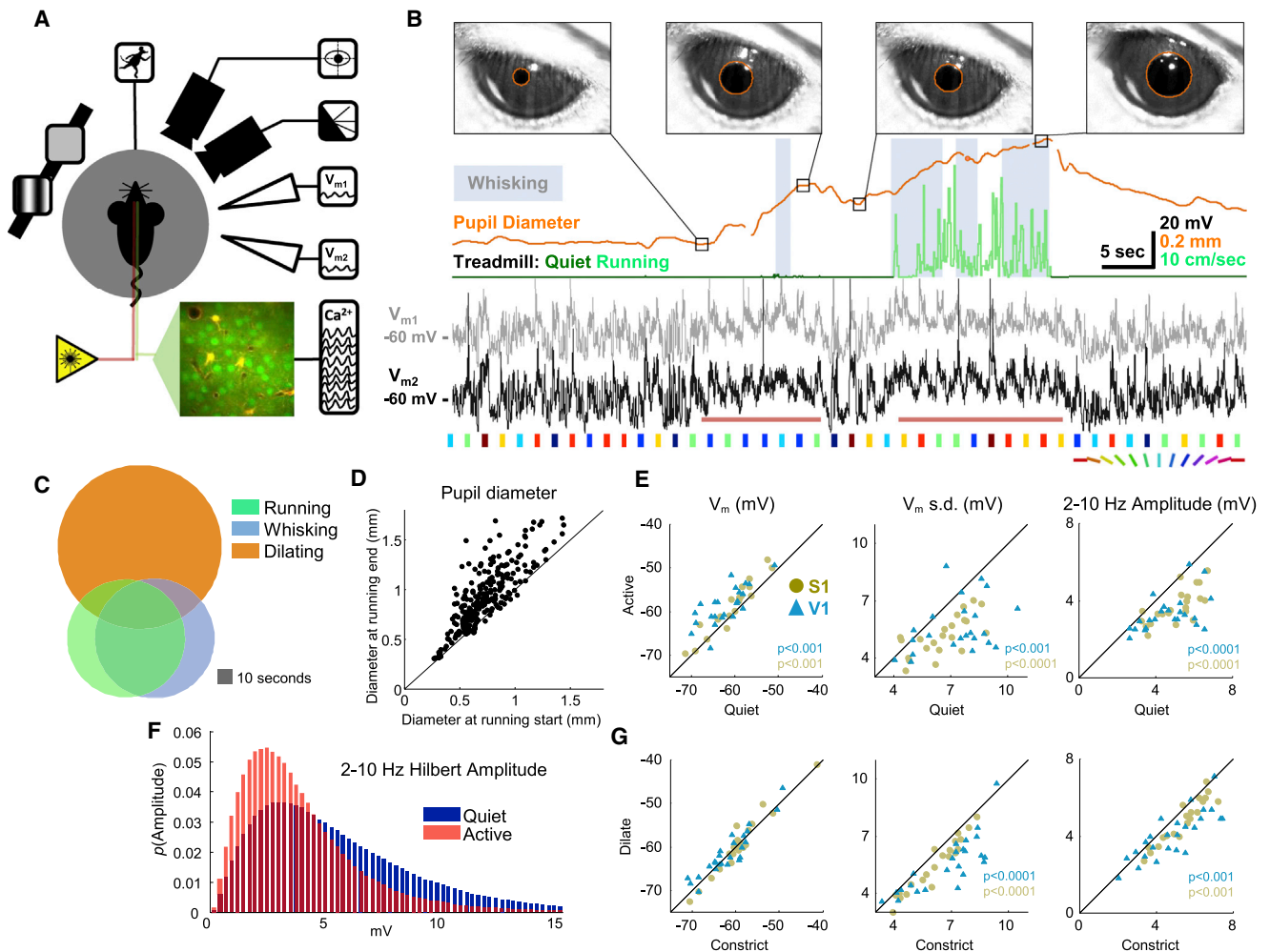
Figure 1. Pupil Diameter, Locomotion, and Whisking Correlate with Subthreshold Measures of Cortical State

(A) Schematic of simultaneous recordings showing mouse on spherical treadmill with eye and whisker cameras, single- or dual-patch pipettes, calcium imaging, and visual stimuli.

(B) Example treadmill activity (running periods in light green, see Supplemental Experimental Procedures), pupil diameter (orange), whisking (light blue background, see Supplemental Experimental Procedures), and V_m from two simultaneously patched cells (black and gray; depolarization around whisking and running epochs indicated with horizontal red lines). Colored patches below the voltage traces indicate presentations of oriented drifting gratings (Figure 4 only). Images of the eye are shown at the time points indicated in the pupil diameter trace, with pupil detection indicated by orange circles. Gaps in the pupil trace are due to blinks.

(C) Overlap of running, whisking, and pupil dilation episodes.

(D) Pupil size before and after running epochs.

(E) Changes in subthreshold membrane potential between quiet wakefulness and activity (running and whisking) without visual stimulation.

(F) Distribution of low-frequency amplitude during active behavior compared to quiet wakefulness.

(G) Changes in subthreshold membrane potential during dilating and constricting epochs of quiet wakefulness, also without visual stimuli. See also Figures S1 and S3 and Movie S1.

together (Figures 1C and S1; Movie S1), consistent with the idea that these behaviors are manifestations of a common exploratory state (Grant et al., 2012). Approximately 90% of these epochs were accompanied by an increase in pupil size (Figures 1B and 1D; mean increase in pupil diameter during running periods 202 ± 11 μm, mean ± SEM; see Experimental Procedures).

Consistent with previous studies (Bennett et al., 2013; Crochet and Petersen, 2006; Niell and Stryker, 2010; Polack et al., 2013; Poulet and Petersen, 2008; Zagha et al., 2013), we found that during exploratory behaviors (running and/or whisking), the

membrane potential (V_m) in both S1 and V1 was desynchronized (red horizontal lines under example V1 recordings in Figure 1B). Relative to quiet wakefulness, V_m in these periods was depolarized (S1: 1.9 ± 0.4 mV, p < 0.001; V1: 3.6 ± 0.7 mV, p < 0.001) and less variable (change in V_m standard deviation, S1: −1.4 ± 0.2 mV, p < 0.0001; V1: −1.7 ± 0.4 mV, p < 0.001), and low-frequency oscillations were reduced (Hilbert amplitude of 2–10 Hz band-pass filtered V_m; S1: −1.4 ± 0.2 mV, p < 0.0001; V1: −1.3 ± 0.2 mV, p < 0.0001; Figure 1E; mean difference ± SEM; Wilcoxon signed-rank test for all comparisons). High-frequency

oscillations in the gamma range were also enhanced during activity compared to quiet wakefulness (Figure S1B), consistent with previous reports (Niell and Stryker, 2010).

During Quiet Epochs, Spontaneous Pupil Fluctuations Are a Sensitive Index of V_m Desynchronization

The large overlap in the amount of synchronous activity during active and quiet periods (Figure 1F) and the reliable increase in pupil size during the desynchronized periods associated with running and whisking led us to ask whether pupil dilation might also be associated with a desynchronized state during quiet wakefulness. To study quiet wakefulness, we excluded periods of running and whisking, and also saccades and blinks, which occurred rarely outside of active behaviors (less than one saccade per minute and less than one blink every 5 min; Figure S1A). We found that during quiet wakefulness, V_m variability was reduced during dilation versus constriction (change in V_m standard deviation, S1: -0.6 ± 0.08 mV, $p < 0.0001$; V1: -1.2 ± 0.2 mV, $p < 0.0001$). This effect could be explained primarily by a reduction in low-frequency oscillations (2–10 Hz Hilbert amplitude; S1: -0.56 ± 0.09 mV, $p < 0.001$; V1: -0.8 ± 0.2 mV, $p < 0.001$; Figure 1G; mean difference $\pm$ SEM; Wilcoxon signed-rank test for all comparisons). A modest increase in V_m oscillations at higher (gamma) frequencies was also observed during dilation compared to constriction (Figure S1C). However, in contrast with the effects of running and whisking, mean V_m was not significantly different for dilation versus constriction.

Pupil fluctuations were much smaller and faster during quiet wakefulness than around bouts of exploratory behavior (Figures 2A–2C; Movies S1 and S2). The duration of individual dilation and constriction periods during quiet wakefulness varied, although in general dilation was faster than constriction (mean dilating duration 1.6 s, mean constricting duration 2.0 s; Figure S2). In order to characterize the time course of the change in synchronous activity relative to pupil fluctuations during quiet wakefulness, we binned the instantaneous 2–10 Hz Hilbert amplitude by the phase of the pupil trace at each time point, aligning multiple cycles of dilation and constriction to one canonical cycle. We found that the amplitude of low-frequency V_m oscillations reached a minimum toward the middle of the dilating phase and peaked during constriction (Figure 2D; plots are mean $\pm$ SEM across cells). Overall, the average intracellular membrane potential was more desynchronized during dilation in both areas S1 and V1 (Figure 2E; S1 and V1, $p < 0.001$; paired t test; bars are mean change during dilation compared to constriction over cells, error bars are SEM; see also Figure S3). This relationship between cortical state and pupil fluctuations persisted even after removing occasional small postural adjustments or whisker twitches from our analysis and after habituating the mice to the treadmill for 30 min per day for 5 days prior to recording (Movie S1; Figure S4).

The robust link between pupil dilation and membrane potential desynchronization in area S1 argues against the possibility of a purely visual effect related to increased illumination of the retina. Although a small number of S1 cells (2/17) were weakly visually responsive (responsiveness generously defined as any significant change in V_m from baseline during a visual stimulus;

$\alpha = 0.05$, Wilcoxon signed-rank test), the majority of visually unresponsive S1 cells still showed a robust relationship between dilation and V_m desynchronization (10/15; Figure 2F). To further rule out the possibility that changes in the visual input alone were responsible for cortical desynchronization, we patched cells in V1 of 8-week- to 4-month-old FVB/NJ (FVB) mice. In these mice, the retinal ganglion cell layer undergoes severe degeneration by P21 (Chang et al., 2002). In contrast to wildtype mice, where most of the V1 cells were visually responsive (12/13), none of the patched cells (0/9) were visually responsive in FVB mice. Yet the relationship between pupil fluctuations and cortical state was also observed in these cells (Figures 2D–2F; $p < 0.05$ Wilcoxon signed-rank test; Figure 2E). We did not observe a significant difference in the effect across the three groups of cells (S1, V1, FVB; one-way ANOVA, $p = 0.53$).

To examine whether state changes were tracked more closely by dilation and constriction or by pupil diameter, we examined the correlation between V_m synchronization and the derivative and absolute size of the pupil (Figures 2G and 2H). We found that the amplitude of 2–10 Hz oscillations was more closely tracked by the derivative than diameter of the pupil (mean fraction of variance explained in a two-way ANOVA for each cell by derivative, 0.13; by diameter, 0.05; $p < 0.0001$, t test).

A Local Interneuron Circuit Participates in the State Changes Tracked by Pupil Fluctuation

Recently, Fu and colleagues found that VIP+ interneurons are activated during running, while SOM+ interneurons are inhibited (Fu et al., 2014), consistent with several recent studies showing that VIP+ cells directly inhibit SOM+ cells, producing a net disinhibition of nearby pyramidal neurons. Furthermore, Fu et al. demonstrated that this cortical circuit was both necessary and sufficient to produce the enhancement of visual responses observed during running.

We initially sought to replicate the effect of active behavior on these interneuron subtypes with targeted patch recordings of labeled VIP+ (n = 6) and SOM+ (n = 30) cells in V1. Consistent with Fu et al., 2014, VIP+ cells were robustly depolarized during running (4.6 $\pm$ 0.8 mV; $p < 0.05$ Wilcoxon signed-rank test; Figures 3B and 3C). However, the behavior of SOM+ cells was more complex. We found that our SOM+ Cre driver line (SST-IRES-Cre; Taniguchi et al., 2011) labeled a population of neurons that could be grouped into two distinct classes, which we call Type I and Type II. Type I SOM+ cells, which were the majority (n = 21/30), exhibited the characteristic low V_m variability described by Petersen and colleagues (Gentet et al., 2012), and these cells were inhibited during active epochs of running and whisking (-2.1 ± 0.47 mV; $p < 0.001$ Wilcoxon signed-rank test; Figures 3A and 3C; Figure S5). A smaller population of Type II-labeled SOM+ cells (n = 7/30) had intrinsic membrane properties more similar to VIP+ or PV+ cells, and these cells were depolarized during active epochs (3.5 $\pm$ 0.9 mV; $p < 0.01$ Wilcoxon signed-rank test; Figure S5). In many cases, we recorded from both types of labeled SOM+ cells in the same animal, and they were completely separable by a number of features, the simplest being the range of voltages spanned by V_m during recordings of spontaneous activity (Figure S5). Both
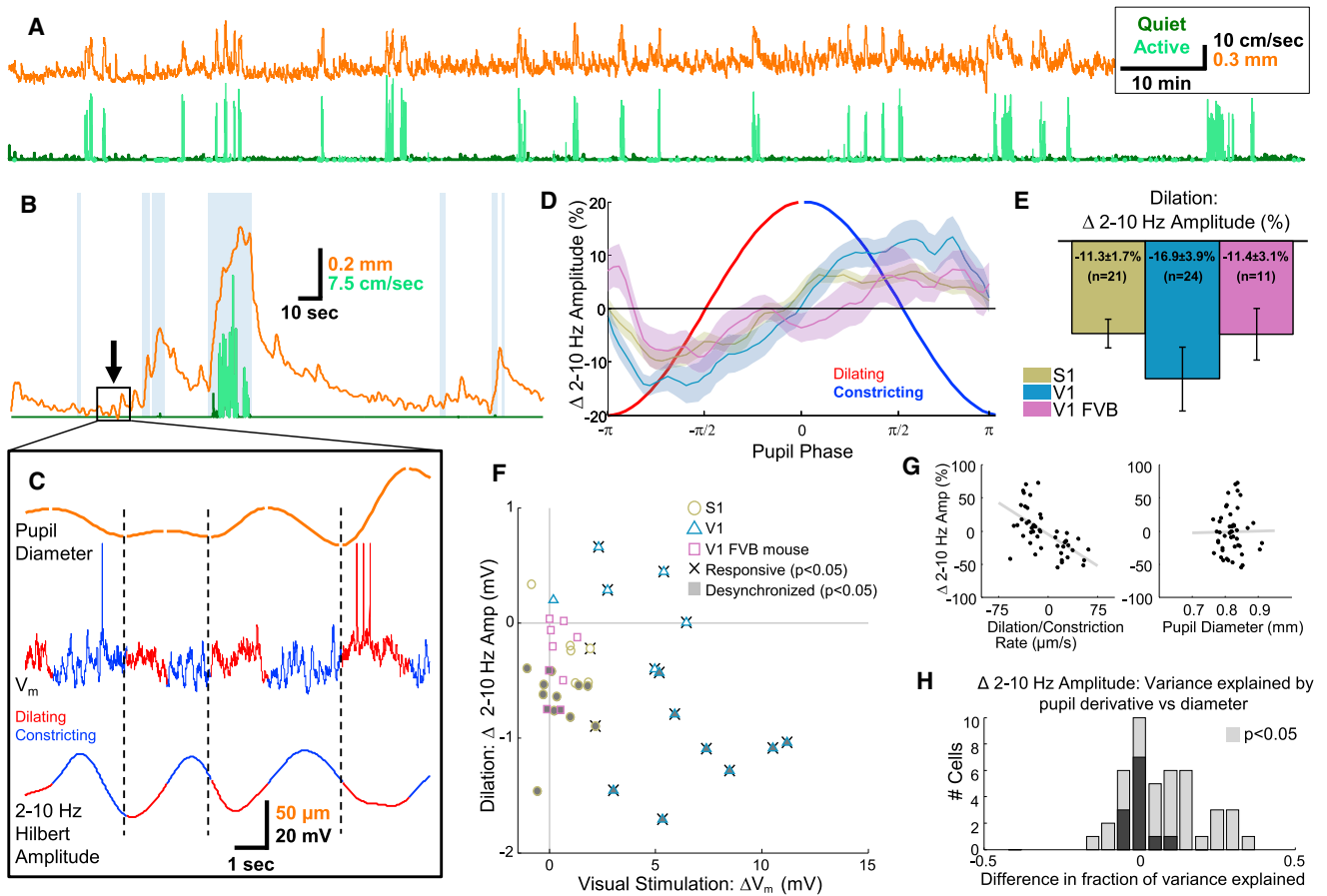
Figure 2. Pupil Diameter Correlates with Cortical State in the Absence of Exploratory Behavior

(A) Concatenated recordings of treadmill speed (running periods in light green, quiet periods in dark green) and pupil diameter (orange) from a single mouse (total time ∼2.4 hr).

(B) Pupil diameter (orange) around a single active period (running in light green and whisking in light blue background).

(C) Zoomed-in period of quiet wakefulness from rectangle in (B) showing four sequential cycles of pupil dilation (red) and constriction (dark blue) correlated with low-frequency amplitude (separate cycles of dilation and constriction separated by dashed vertical lines).

(D) V_m is desynchronized during dilation and synchronized during constriction of the pupil in S1 (olive), V1 (blue), and V1 of FVB mice (mauve; 64 phase bins from $-\pi$ to π, plots are mean ± SEM for each bin).

(E) Averages over entire dilation and constriction periods for cells in each area (bar plots are mean ± SEM across cells, one-way ANOVA across cell groups was not significant p = 0.53).

(F) Scatterplot of desynchronization during dilation and visual responsiveness for all cells in each area. Significantly responsive cells are indicated with whiskers; significantly desynchronized cells are indicated with shading.

(G) Linear regression of the rate of change (left) and the absolute value of pupil diameter (right) against percent change in 2–10 Hz amplitude for a single cell.

(H) Stacked histogram of the difference in total variance in 2–10 Hz amplitude explained by pupil derivative and pupil diameter in a two-way ANOVA for each cell. Cells where either factor was significant (p < 0.05) are indicated with lighter bars. Overall, variations in cortical state indexed by low-frequency amplitude are more closely tracked by pupil dilation and constriction than by absolute pupil diameter (p < 0.0001, t test). See also Figures S2–S4 and Movie S2.

SOM+ Type I and Type II cells were distinct from morphologically identified (spiny) pyramidal cells, which were rarely labeled (n = 2/56), presumably due to leaky expression of Cre recombinase (Figure S5). Although the fact that the widely used SST-IRES-Cre line (Taniguchi et al., 2011) labels subpopulations of interneurons with different in vivo functional properties has not been previously reported, a recent in vitro study using these mice found two electrophysiologically distinct populations of labeled cells in almost the same proportions that we observed here (Hu et al., 2013). Based on these findings, we excluded Type II SOM+ cells in subsequent analyses.

Having confirmed the results of Fu et al. with respect to running, we wondered whether the SOM+/VIP+ cortical circuit might also participate in the state changes indexed by dilation and constriction during quiet wakefulness. Indeed, we found that VIP+ cells were relatively depolarized during dilation (2.1 ± 0.6 mV, p < 0.05) while SOM+ cells were hyperpolarized (−0.7 ± 0.3mV, p < 0.05; Wilcoxon signed-rank test for all comparisons; Figures 3D and 3E). Our results support the view that the SOM+/VIP+ circuit is not only recruited during active behavior, but may also play a role in cortical state changes during quiet wakefulness.
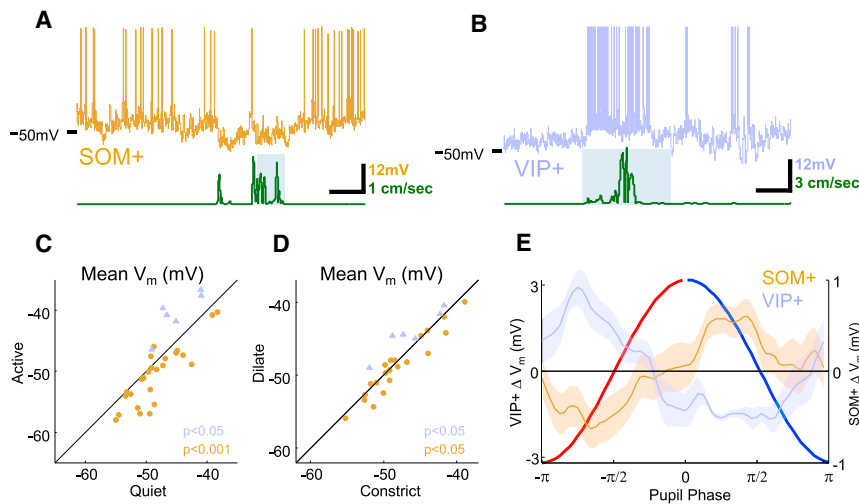
Figure 3. VIP+ Cells Are Excited and SOM+ Cells Are Inhibited during Active Behaviors and during Dilation

(A) Example SOM+ cell (brown) and treadmill (green) trace with whisking epoch as light blue rectangles in background. SOM+ cells are hyperpolarized during locomotion.

(B) Example VIP+ cell (blue) and treadmill (green) trace with whisking epoch as gray background. VIP+ activity is dramatically enhanced during running.

(C) Inhibition of SOM+ and excitation of VIP+ during exploratory behaviors compared to quiet wakefulness.

(D) In quiet wakefulness, SOM+ cells are inhibited and VIP+ cells are excited during dilation compared to constriction.

(E) Phase-binned change in SOM+ and VIP+ V_m showing time course of signature opposition of VIP+ and SOM+ activity over dilating and constricting periods (error bands are SEM).

Visual Encoding Is Improved during Desynchronized States Defined by Pupil Dilation

To determine whether stimulus encoding in V1 is improved during the desynchronized state indexed by pupil dilation, we performed two-photon calcium imaging of populations of layer 2/3 cells loaded with the calcium-sensitive fluorescent indicator Oregon Green BAPTA-1AM while presenting drifting oriented gratings (example site, Figures 4A and 4B; n = 34 imaging sites in six mice). We analyzed cells that were tuned for orientation (1,200/3,435 cells significantly tuned; see Experimental Procedures). During exploratory activity (running and whisking), there was a 20% increase in the mean response to preferred direction (p < 10^{-12}) and a 19% increase in the mean response to orthogonal directions (p < 10^{-15}; n = 516 tuned cells in 14 sites with sufficient numbers of visual responses during both active behavior and quiet wakefulness). These changes resulted in a slight decrease in orientation selectivity, but consistent with previous reports (Niell and Stryker, 2010; Polack et al., 2013), this change was not significant (7% decrease in OSI, p = 0.07; Figure 4C, error bands are SEM across cells). During quiet wakefulness, with running, whisking, and saccades removed, dilation was associated with a 9% increase in the mean response to preferred direction (p < 10^{-13}) and no change (0.6%, p = 0.47) in the response to the orthogonal direction, resulting in an enhancement of orientation selectivity (Figures 4D and 4E; 16% increase in OSI, p < 10^{-6}). Note that there was no significant difference in the size of the pupil between dilating and constricting trials (Figure S6). During dilation, responses to drifting gratings were also more reliable (Figure 4F; 28% increase in mean variability explained by stimulus conditions, p < 10^{-15}; n = 619 cells in 22 sites). Although there are a number of caveats that make it difficult to estimate the *absolute* magnitude of noise correlations using calcium imaging data (Cotton et al., 2013), we found that the relative magnitude of correlated activity varied significantly between the two states. There was a decrease in both signal and noise correlations during dilation versus constriction (Figures 4G and 4H; 20% decrease in mean noise correlations, p < 0.0001 and 16% decrease in mean signal correlations, p < 0.01; n = 21 sites,

paired t test used for all comparisons; see Experimental Procedures). In summary, we found that responses to drifting gratings were more selective, more reliable, and less correlated during dilation compared to constriction.

We next asked whether visual encoding of natural stimuli was also enhanced during desynchronized states indexed by pupil dilation. We presented multiple repetitions of short prerecorded movies from a head-mounted camera of a mouse navigating an enriched environment. We performed calcium imaging in V1 (n = 53 imaging sites in seven mice). In addition to excluding running and whisking periods, we also removed saccades and any epochs where the eye deviated by more than 10° from its mean position. Correlating neural activity directly with changes in pupil size was not possible in this experiment because differences in brightness across frames elicited reliable dilations and constrictions of the pupil across multiple repetitions of the movie (r = 0.61 correlation of pupil size across trials for one example recording session, Figure 5A). To account for the effects of frame-to-frame changes in luminance, we sorted the responses to each 150 ms segment of the movie by the rate of change of pupil diameter and compared the neural responses for the upper and lower quartiles of the rates of change within each time bin (Figure 5B). Here, we assumed that the average change in pupil size over multiple movie repetitions (gray trace in Figure 5B) was due to luminance changes in the stimulus, while the variability around this average (blue and red vertical lines in Figure 5B) reflected the trial-to-trial differences in cortical state. Thus, for each bin, we compared "high" trials, when the pupil was dilating faster than usual (or constricting slower than usual) to "low" trials, when the pupil was dilating slower (or constricting faster) than the average.

Visual responses were enhanced during high trials compared to low trials (example cell in Figure 5C). Consistent with the increased OSI we observed for oriented gratings, responses to preferred frames of the movie were selectively enhanced during high trials compared to low trials (Figures 5D and 5E). Again, the pupil was not larger during high trials than low trials (Figure S6). At the population level, both signal (Figure 5F; p < 0.001) and
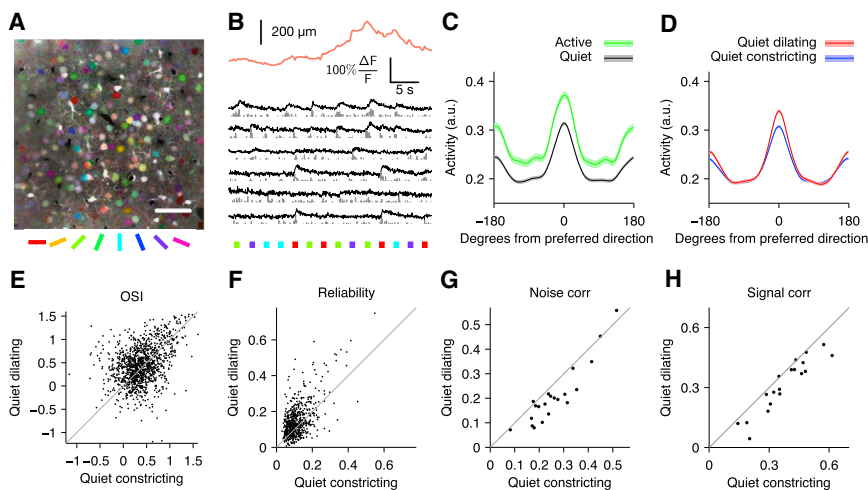
Figure 4. Orientation Tuning Is Enhanced during Pupil Dilation

(A) Mean fluorescence image colored by orientation preferences of individual pixels; scale bar, 50 μm.

(B) Example pupil diameter trace (orange) with simultaneous calcium traces from segmented cells (black) and inferred firing rates (gray). Colored squares indicate the direction of drifting gratings.

(C) Average tuning curves aligned to cells' preferred direction for active (running and/or whisking) periods (green) and quiet (black) periods. Peak responses are increased (20%, $p < 10^{-12}$) and orientation selectivity is unchanged (7% decrease, $p = 0.07$). Error bands are SEM computed over cells ($n = 516$).

(D) Average tuning during pupil dilation (red) and constriction (blue) during quiet periods (excluding running and whisking).

(E–H) Orientation selectivity is increased during dilation compared to constriction (16% increase in mean OSI, $p < 10^{-6}$) (E). Cells also respond more reliably during dilation compared to constriction (28% increase in mean binned R^2 values of stimulus responses of individual cells, $p < 10^{-15}$) (F). Across populations of neurons, mean noise correlations (G) ($p < 10^{-4}$) and signal correlations (H) ($p < 0.01$) are reduced during pupil dilation ($n = 21$ sites). Paired t test for all comparisons. Reliability and correlations are computed on 150 ms bins during stimulus presentations (see Supplemental Experimental Procedures).

noise (Figure 5G; $p < 0.05$) correlations were reduced, and there was an increase in the reliability (Figure 5H; $p < 0.001$) and discriminability (Figure 5I; $p < 0.001$) of responses during high trials compared to low trials (t test for all comparisons). In summary, consistent with the enhancement of responses to drifting gratings during dilation, responses to natural movies were more selective, more reliable, and less correlated during high trials.

DISCUSSION

We performed whole-cell patching and two-photon calcium imaging in awake mice (Bennett et al., 2013; Niell and Stryker, 2010; Polack et al., 2013) and focused our analysis on quiet periods between epochs of running and whisking. During these periods, we observed small spontaneous fluctuations in pupil diameter on a timescale of 1–2 s, which tracked changes in intracellular dynamics of L2/3 neurons in both somatosensory (S1) and visual (V1) cortex. V_m was desynchronized while the pupil was dilating and was dominated by low-frequency oscillations while the pupil was constricting. Dilation was accompanied by activation of VIP+ and inhibition of SOM+ interneurons, a phenomenon that has been shown to be essential to the enhanced visual responses observed during running (Fu et al., 2014). Using two-photon calcium imaging, we found that dilation was associated with an enhancement of visual responses and a reduction in both noise and signal correlations across ensembles of neurons for both gratings and natural stimuli.

For almost half a century, pupillometry has been widely used to index covert changes in attention and effort in humans and nonhuman primates (Gilzenrat et al., 2010; Hess and Polt, 1960, 1964; Iriki et al., 1996; Kahneman, 1973; Kahneman and Beatty, 1966; Kristjansson et al., 2009; Onorati et al., 2013; Wierda et al., 2012). Surprising and provocative stimuli produce a transient increase in pupil size (Bradley et al., 2008; Hess and Polt, 1960, 1964; Libby et al., 1973; Preuschoff et al., 2011), and

pupil dilation preceding stimulus onset is correlated with faster reaction times in psychophysical tasks (Kristjansson et al., 2009). Our results provide evidence of changes in intracellular membrane potential dynamics and neural population activity underlying these psychophysical effects and emphasize the utility of pupil dilation and constriction as a proxy for noninvasively monitoring internal cortical states.

Previous authors have pointed out the analogy between desynchronization and enhanced sensory encoding during attention in primates, and the changes in cortical state during exploratory behaviors in mice (Harris and Thiele, 2011). Our results suggest that this analogy may be extended further, to encompass fluctuations in brain state in mice in the absence of overt behavioral changes. The ability to leverage mouse genetics to study the mechanisms that produce these state changes will be valuable, as will the ability to examine the potential dysregulation of brain state in mouse models of human disease.

Intracellular signatures of cortical activation were linked to pupil dilation across multiple cortical areas, suggesting that the effects we observe reflect a global change in brain state. Given the close relationship between pupil diameter, locus coeruleus activity, and sympathetic tone (Aston-Jones et al., 1999; Bradley et al., 2008; Gilzenrat et al., 2010), our data suggest a role for norepinephrine in the regulation of cortical state. Consistent with this notion, a recent study has implicated norepinephrine in the desynchronization that occurs during running (Polack et al., 2013). However, the potential contribution of other neuromodulators such as acetylcholine (Goard and Dan, 2009; Pinto et al., 2013) is also strongly suggested by the fact that the VIP+ activation during running has been shown to depend on cholinergic input from the diagonal band of Broca (Fu et al., 2014).

Additional mechanisms may also contribute to the state changes we describe here, which differ in at least two important ways from the state associated with exploratory behavior: First, unlike the effects of running, the desynchronization during
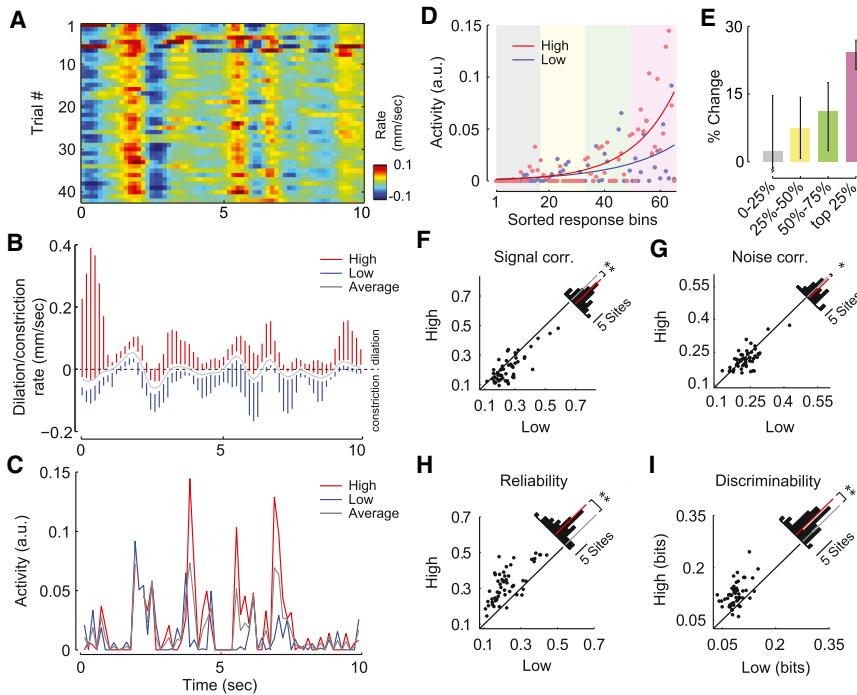
Figure 5. Encoding of Natural Images Is Improved during Pupil Dilation

(A) Pupil dilation/constriction rates across multiple repetitions of a natural movie.

(B) Mean (gray) and range in upper and lower quartiles (red and blue, respectively) of the pupil dilation/constriction rate for multiple presentations of a single movie (150 ms bins). Subsequent analyses compare neural responses in the upper quartile of pupil dilation/constriction rates ("high") to the lower quartile ("low").

(C) Increase in mean activity during high trials compared to low trials for a single cell.

(D) For each cell, movie frames are sorted by the mean neural response, not considering pupil dilation and constriction. Responses in high (red dots) and low (blue dots) conditions are fit with an exponential function (solid red and blue lines) to illustrate the selective increase in response to preferred stimuli.

(E) Median change in firing rate in high trials compared to low trials (n = 467 neurons, 95% confidence intervals) for least preferred (0%–25%), intermediate (25%–50% and 50%–75%), and most-preferred (75%–100%) frames for each cell. Responses to preferred frames are selectively enhanced.

(F–I) Mean signal (F) and noise (G) correlations decreased during the high condition, while reliability (H) and discriminability (I) were enhanced. Insets show histograms of absolute change with red bar indicating the mean difference (n = 53 sites, **p < 0.001, *p < 0.05, t test).

dilation is not accompanied by a significant depolarization of V_m. Second, we observe a qualitative difference in the effect of state on orientation tuning. During running, visual responses are enhanced at all orientations, while during dilation, responses at preferred orientations are enhanced without changing responses at orthogonal orientations, resulting in an increase in orientation selectivity. Further work will be necessary to uncover the mechanisms underlying these differences.

It is interesting to consider the potential computational role of continuous fluctuations in state during behaviorally quiescent periods. We speculate that during quiet wakefulness, the cortex may rapidly alternate between two distinct modes of information processing: a desynchronized state characterized by improved representation of feedforward sensory information and a synchronized state dominated by internally generated low-frequency network oscillations. Interestingly, theoretical work has suggested that alternating between bottom-up and top-down processing may be an efficient learning mechanism for the cortex to build a representation of the external world (Hinton, 2010).

EXPERIMENTAL PROCEDURES

All procedures were approved by the Institutional Animal Care and Use Committee (IACUC) of Baylor College of Medicine. Briefly, mice were anesthetized and a 3 mm craniotomy was made over the cortex as previously described (Froudarakis et al., 2014). For calcium imaging experiments, OGB1-AM was injected before sealing the craniotomy with a glass coverslip, which in some cases was prepared with a small (~500 μm) hole to allow pipette access. Following surgery, the mouse was placed on a treadmill with its head restrained beneath the microscope objective. Locomotion was detected by treadmill movement, and eye and whisker movements were detected optically. Whole-cell in vivo patching was performed using borosilicate patch pipettes (6–10

MΩ) filled with a standard low Cl⁻ internal solution (Jiang et al., 2013) as well as Alexa 488 or 598 for visualization. Visual stimuli were as follows: Figures 1, 2, and 3, blank screen; Figure 4, full-field square wave gratings (0.04 cycles/degree at 2 Hz, 500 ms trials interleaved with 1 s luminance-matched blanks, 100 repeats x 8 orientations); Figure 5, natural scene movies collected as previously described (Froudarakis et al., 2014). Calcium imaging was performed using either a standard galvo-galvo (Sutter Instruments) or resonant scanner (Thor Labs) using a Ti-Sapphire laser (Coherent) exciting at either 800 or 1,000 nm and equipped with either a 20× (1.0 NA, Olympus) or 25× (1.1 NA, Nikon) objective lens. Imaging data were motion-corrected and cell segmentation was manually supervised. A more detailed description of all experimental procedures can be found online in our Supplemental Experimental Procedures.

SUPPLEMENTAL INFORMATION

Supplemental Information includes Supplemental Experimental Procedures, six figures, and two movies and can be found with this article online at http://dx.doi.org/10.1016/j.neuron.2014.09.033.

AUTHOR CONTRIBUTIONS

ACKNOWLEDGMENTS

REFERENCES

Aston-Jones, G., Rajkowski, J., and Cohen, J. (1999). Role of locus coeruleus in attention and behavioral flexibility. Biol. Psychiatry *46*, 1309–1320.

Bennett, C., Arroyo, S., and Hestrin, S. (2013). Subthreshold mechanisms underlying state-dependent modulation of visual responses. Neuron *80*, 350–357.

Bradley, M.M., Miccoli, L., Escrig, M.A., and Lang, P.J. (2008). The pupil as a measure of emotional arousal and autonomic activation. Psychophysiology *45*, 602–607.

Chang, B., Hawes, N.L., Hurd, R.E., Davisson, M.T., Nusinowitz, S., and Heckenlively, J.R. (2002). Retinal degeneration mutants in the mouse. Vision Res. *42*, 517–525.

Colten, H.R., and Altevogt, B.M., eds. (2006). Sleep Disorders and Sleep Deprivation: An Unmet Public Health Problem (Washington, DC: National Academies Press).

Cotton, R.J., Froudarakis, E., Storer, P., Saggau, P., and Tolias, A.S. (2013). Three-dimensional mapping of microcircuit correlation structure. Front Neural Circuits *7*, 151.

Crochet, S., and Petersen, C.C.H. (2006). Correlating whisker behavior with membrane potential in barrel cortex of awake mice. Nat. Neurosci. *9*, 608–610.

Froudarakis, E., Berens, P., Ecker, A.S., Cotton, R.J., Sinz, F.H., Yatsenko, D., Saggau, P., Bethge, M., and Tolias, A.S. (2014). Population code in mouse V1 facilitates readout of natural scenes through increased sparseness. Nat. Neurosci. *17*, 851–857.

Fu, Y., Tucciarone, J.M., Espinosa, J.S., Sheng, N., Darcy, D.P., Nicoll, R.A., Huang, Z.J., and Stryker, M.P. (2014). A cortical circuit for gain control by behavioral state. Cell *156*, 1139–1152.

Gentet, L.J., Kremer, Y., Taniguchi, H., Huang, Z.J., Staiger, J.F., and Petersen, C.C.H. (2012). Unique functional properties of somatostatin-expressing GABAergic neurons in mouse barrel cortex. Nat. Neurosci. *15*, 607–612.

Gilzenrat, M.S., Nieuwenhuis, S., Jepma, M., and Cohen, J.D. (2010). Pupil diameter tracks changes in control state predicted by the adaptive gain theory of locus coeruleus function. Cogn. Affect. Behav. Neurosci. *10*, 252–269.

Goard, M., and Dan, Y. (2009). Basal forebrain activation enhances cortical coding of natural scenes. Nat. Neurosci. *12*, 1444–1449.

Gould, I.C., Rushworth, M.F., and Nobre, A.C. (2011). Indexing the graded allocation of visuospatial attention using anticipatory alpha oscillations. J. Neurophysiol. *105*, 1318–1326.

Grant, R.A., Mitchinson, B., and Prescott, T.J. (2012). The development of whisker control in rats in relation to locomotion. Dev. Psychobiol. *54*, 151–168.

Grent-'t-Jong, T., Boehler, C.N., Kenemans, J.L., and Woldorff, M.G. (2011). Differential functional roles of slow-wave and oscillatory-α activity in visual sensory cortex during anticipatory visual-spatial attention. Cereb. Cortex *21*, 2204–2216.

Harris, K.D., and Thiele, A. (2011). Cortical state and attention. Nat. Rev. Neurosci. *12*, 509–523.

Hei, X., Stoelzel, C.R., Zhuang, J., Bereshpolova, Y., Huff, J.M., Alonso, J.M., and Swadlow, H.A. (2014). Directional selective neurons in the awake LGN: response properties and modulation by brain state. J. Neurophysiol. *112*, 362–373.

Hess, E.H., and Polt, J.M. (1960). Pupil size as related to interest value of visual stimuli. Science *132*, 349–350.

Hess, E.H., and Polt, J.M. (1964). Pupil Size in Relation to Mental Activity during Simple Problem-Solving. Science *143*, 1190–1192.

Hinton, G.E. (2010). Learning to represent visual input. Philos. Trans. R. Soc. Lond. B Biol. Sci. *365*, 177–184.

Hu, H., Cavendish, J.Z., and Agmon, A. (2013). Not all that glitters is gold: off-target recombination in the somatostatin-IRES-Cre mouse line labels a subset of fast-spiking interneurons. Front Neural Circuits *7*, 195.

Iriki, A., Tanaka, M., and Iwamura, Y. (1996). Attention-induced neuronal activity in the monkey somatosensory cortex revealed by pupillometrics. Neurosci. Res. *25*, 173–181.

Jiang, X., Wang, G., Lee, A.J., Stornetta, R.L., and Zhu, J.J. (2013). The organization of two new cortical interneuronal circuits. Nat. Neurosci. *16*, 210–218.

Kahneman, D. (1973). Attention and Effort. (Englewood Cliffs, NJ: Prentice-Hall Inc.).

Kahneman, D., and Beatty, J. (1966). Pupil diameter and load on memory. Science *154*, 1583–1585.

Kristjansson, S.D., Stern, J.A., Brown, T.B., and Rohrbaugh, J.W. (2009). Detecting phasic lapses in alertness using pupillometric measures. Appl. Ergon. *40*, 978–986.

Lee, S.-H., and Dan, Y. (2012). Neuromodulation of brain states. Neuron *76*, 209–222.

Libby, W.L., Jr., Lacey, B.C., and Lacey, J.I. (1973). Pupillary and cardiac activity during visual attention. Psychophysiology *10*, 270–294.

Niell, C.M., and Stryker, M.P. (2010). Modulation of visual responses by behavioral state in mouse visual cortex. Neuron *65*, 472–479.

Onorati, F., Barbieri, R., Mauri, M., Russo, V., and Mainardi, L. (2013). Characterization of affective states by pupillary dynamics and autonomic correlates. Front Neuroeng *6*, 9.

Pinto, L., Goard, M.J., Estandian, D., Xu, M., Kwan, A.C., Lee, S.H., Harrison, T.C., Feng, G., and Dan, Y. (2013). Fast modulation of visual perception by basal forebrain cholinergic neurons. Nat. Neurosci. *16*, 1857–1863.

Polack, P.-O., Friedman, J., and Golshani, P. (2013). Cellular mechanisms of brain state-dependent gain modulation in visual cortex. Nat. Neurosci. *16*, 1331–1339.

Poulet, J.F.A., and Petersen, C.C.H. (2008). Internal brain state regulates membrane potential synchrony in barrel cortex of behaving mice. Nature *454*, 881–885.

Preuschoff, K., 't Hart, B.M., and Einhäuser, W. (2011). Pupil Dilation Signals Surprise: Evidence for Noradrenaline's Role in Decision Making. Front Neurosci *5*, 115.

Rohenkohl, G., and Nobre, A.C. (2011). α oscillations related to anticipatory attention follow temporal expectations. J. Neurosci. *31*, 14076–14084.

Taniguchi, H., He, M., Wu, P., Kim, S., Paik, R., Sugino, K., Kvitsiani, D., Fu, Y., Lu, J., Lin, Y., et al. (2011). A resource of Cre driver lines for genetic targeting of GABAergic neurons in cerebral cortex. Neuron *71*, 995–1013.

Wierda, S.M., van Rijn, H., Taatgen, N.A., and Martens, S. (2012). Pupil dilation deconvolution reveals the dynamics of attention at high temporal resolution. Proc. Natl. Acad. Sci. USA *109*, 8456–8460.

Zagha, E., Casale, A.E., Sachdev, R.N., McGinley, M.J., and McCormick, D.A. (2013). Motor cortex feedback influences sensory processing by modulating network state. Neuron *79*, 567–578.

Zhuang, J., Bereshpolova, Y., Stoelzel, C.R., Huff, J.M., Hei, X., Alonso, J.M., and Swadlow, H.A. (2014). Brain state effects on layer 4 of the awake visual cortex. J. Neurosci. *34*, 3888–3900.

Supplemental Information

Pupil Fluctuations Track Fast Switching
of Cortical States during Quiet Wakefulness

Jacob Reimer, Emmanouil Froudarakis, Cathryn R. Cadwell,
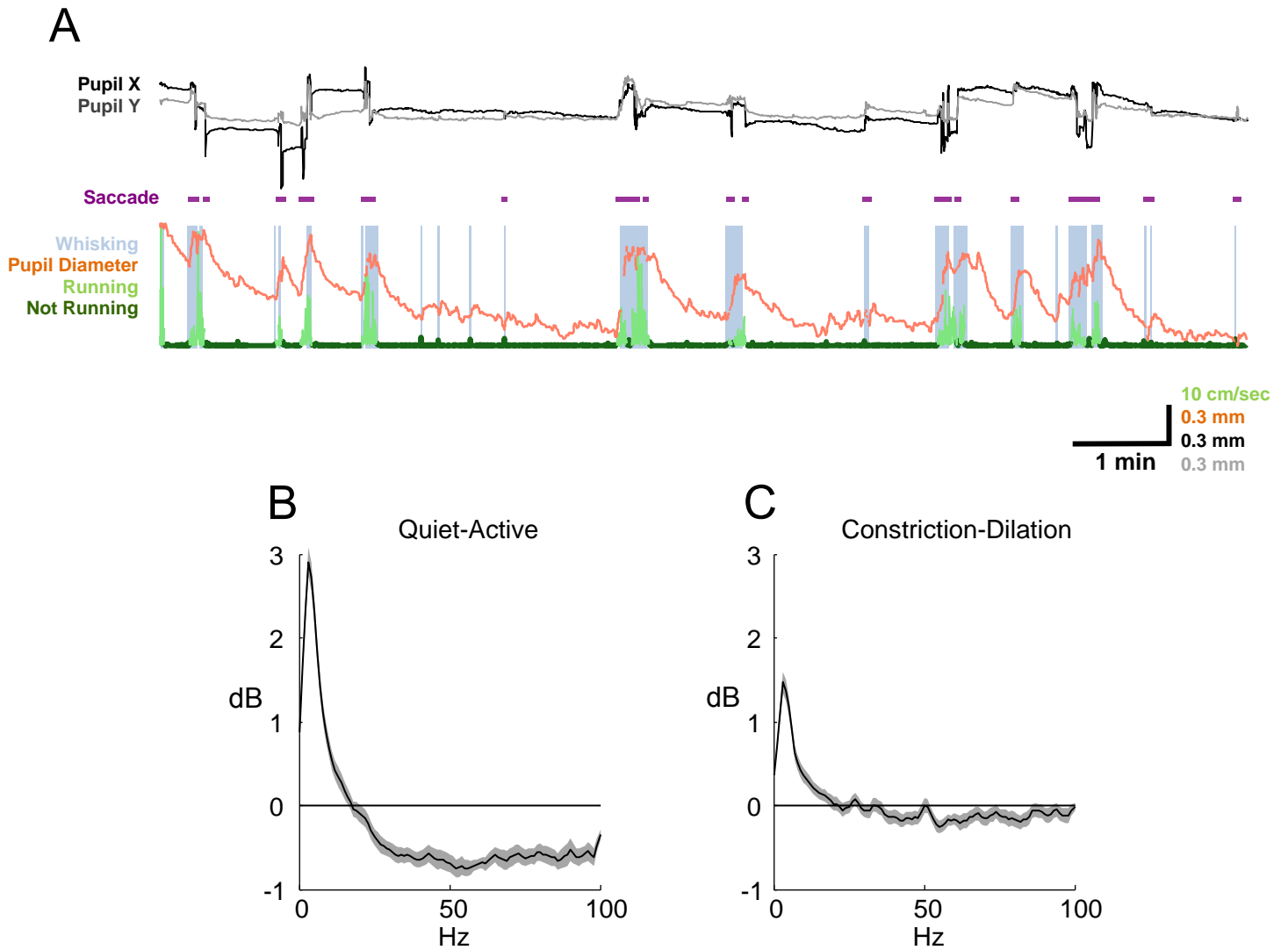Dimitri Yatsenko, George H. Denfield, and Andreas S. Tolias

Supplemental Data

A

B   Quiet-Active

C   Constriction-Dilation

Figure S1, related to Figure 1. Saccades and power spectra during running and quiet wakefulness.

(**A**) Example traces of simultaneously recorded treadmill speed (running in light green, quiet in dark green), pupil size (orange), whisking periods (blue rectangles) and horizontal (x, black) and vertical (y, gray) eye movements. Detected saccades are indicated in purple below the

position traces. Saccades are much more frequent during running. Brief periods of missing data in the pupil diameter is due to blinks or frames where the exact diameter and position of the pupil could not be defined due to blurring during a saccade. (**B**) Ratio of mean V_m power spectra between quiet wakefulness and active periods of whisking and running. Lower-frequency oscillations are enhanced during quiet wakefulness, especially in the 2-10 Hz range; and there is a wide-band increase in gamma frequencies during active behavior. (V_m power spectra for each condition estimated using Welch's method; mean ± SEM over n=52 cells from both S1 and V1). (**C**) Ratio of mean power spectra during constriction and dilation in quiet wakefulness. Power in the lower frequencies in the 2-10 Hz range is higher during constriction, and there is a modest wide-band power increase in higher gamma frequencies during dilation (mean ± SEM, n=54 cells).
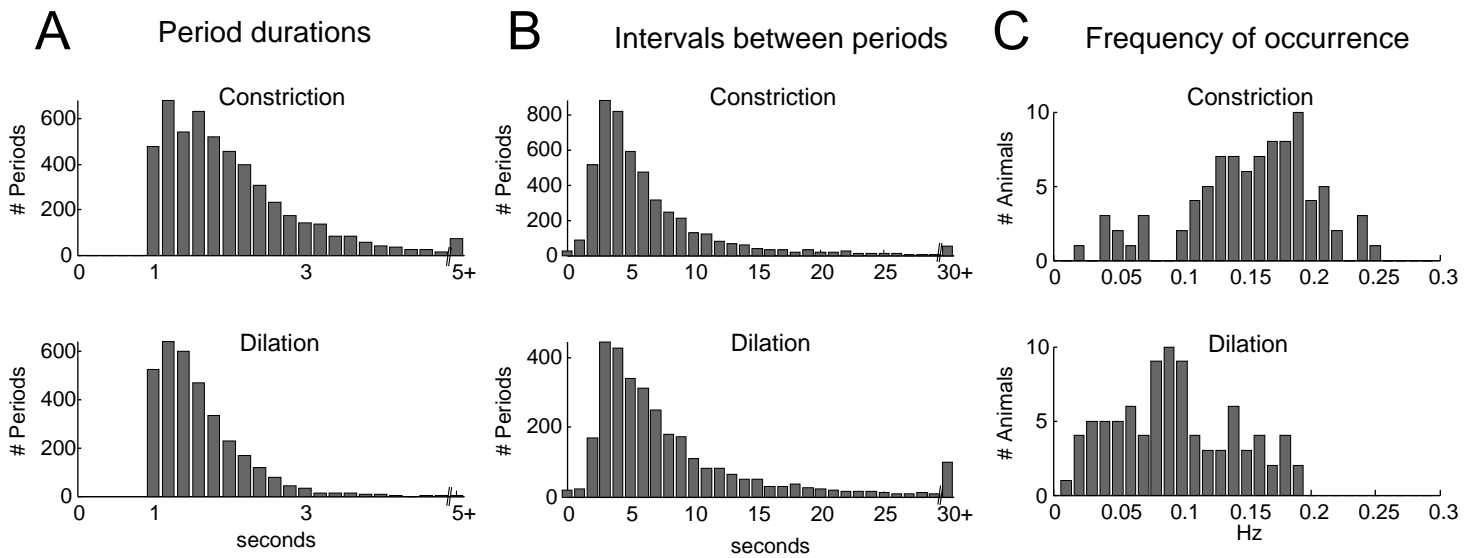
Figure S2, related to Figure 2. Temporal characteristics of dilating and constricting periods during quiet wakefulness.

Dilation and constriction periods were defined by extrema in the low-pass (4th order Butterworth, 1 Hz cutoff) filtered pupil trace. Only periods lasting more than one second with an absolute mean dilation or constriction rate greater than 10 μm/s are included in this figure and all our analyses, as our ability to reliably detect fluctuations smaller than this was limited by the shape and sharpness of the pupil boundary and the camera's resolution and frame rate. These periods comprised approximately 55% of our recordings during quiet wakefulness, and removing this threshold did not qualitatively change our findings. (**A**) Histogram of detected period durations. In general, constricting periods (top) were longer in duration (mean: 2.0 s, median 1.8 s) than dilating periods (bottom; mean: 1.6 s, median 1.5 s). (**B**) Histogram of intervals between sequential detected constricting (top) and dilating (bottom) periods (mean interval between constriction periods: 6.3 s, median: 4.6 s; mean interval between dilation periods: 8.4 s, median: 5.8 s). (**C**) Histogram of average frequency of detected constricting (top)

and dilating (bottom) periods for n=84 mice, including some animals not used elsewhere in this study. On average during quiet wakefulness, constricting periods were detected at approximately 0.15 Hz while dilating periods were detected at approximately 0.09 Hz.
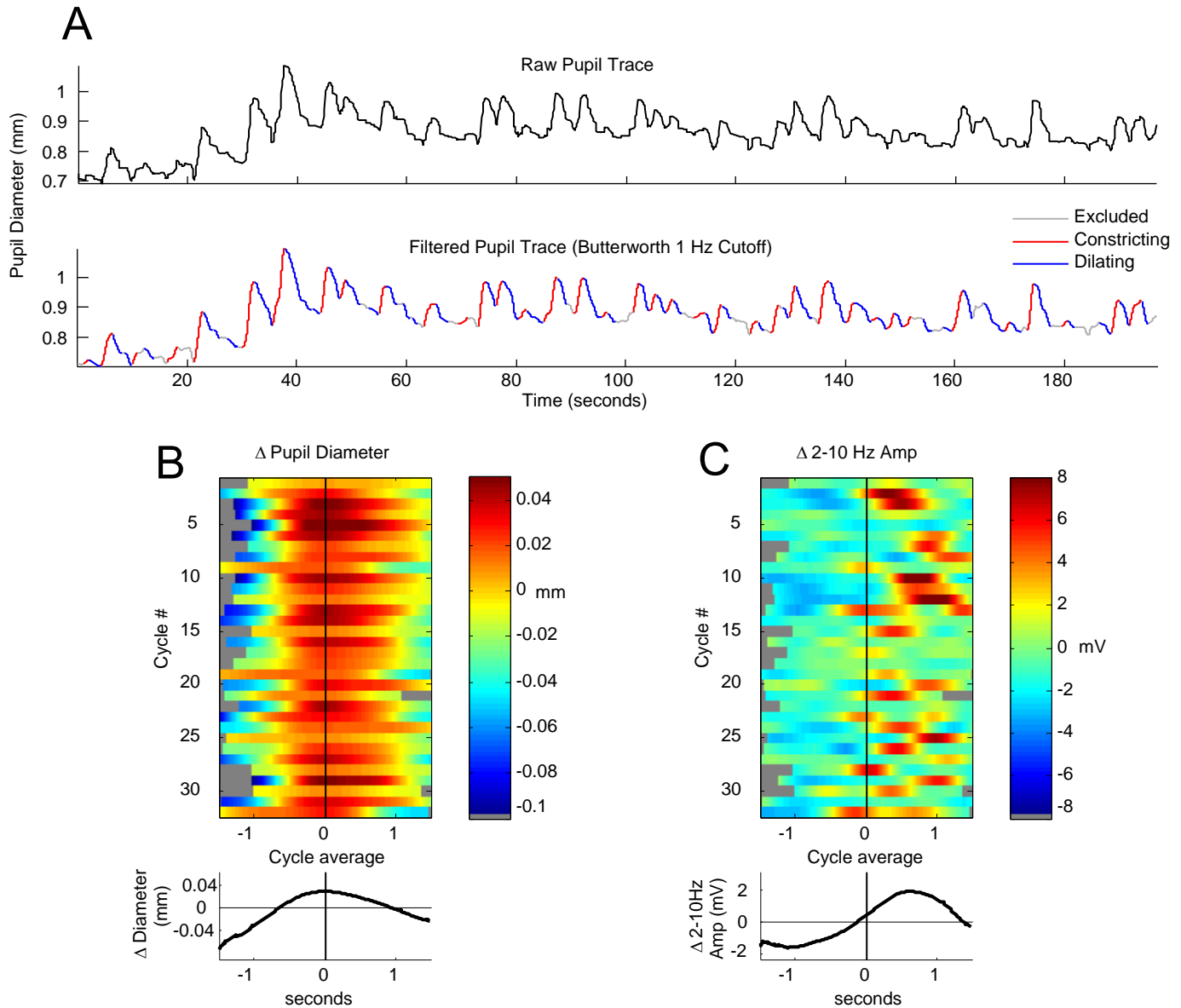
Figure S3, related to Figure 2. Single-cell example of raw data showing state change over multiple cycles of dilation and constriction.

(**A**) Unfiltered continuous trace of pupil diameter over time (top), and filtered trace (bottom). Dilating (red), constricting (blue), and excluded (grey) periods are indicated on filtered trace. (**B, top**) Change in pupil diameter for consecutive individual dilation and constriction cycles from trace in (**A**). (**B, bottom**) Mean change in pupil diameter averaged over all cycles. (**C, top**)

Corresponding segments of 2-10 Hz Hilbert amplitude. Entire Hilbert amplitude trace is band-pass filtered between 0.1 Hz and 1 Hz, and segments are collected corresponding to each cycle in (**B**). (**C, bottom**) Mean 2-10 Hz amplitude change averaged over all cycles. Note the similarity in the mean change in 2-10 Hz amplitude for this single cell example with the phase-binned average in Figure 2D.
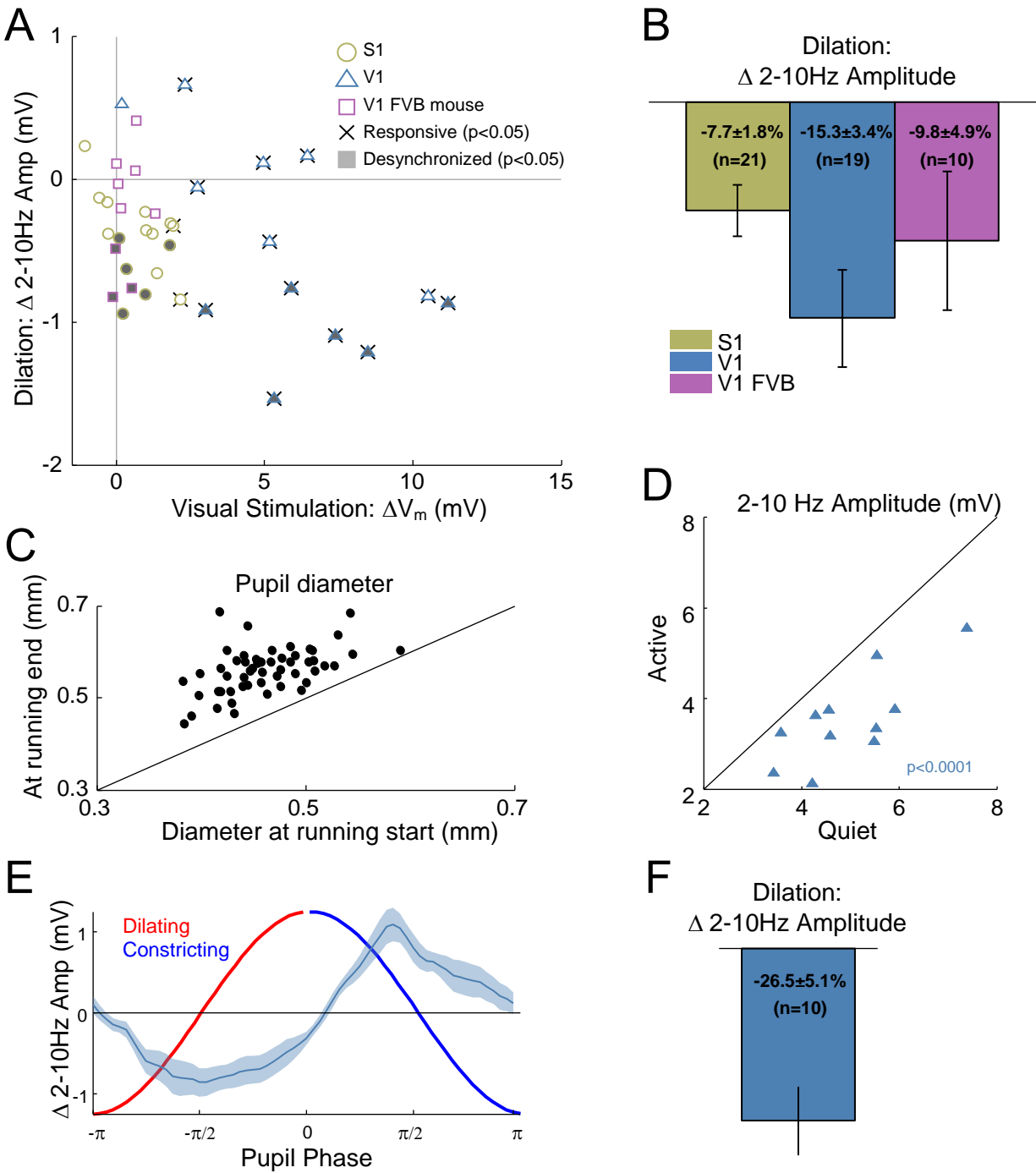
Figure S4, related to Figures 1 and 2. Relationship between pupil dilation and Vₘ dynamics persists when small whisker or treadmill movements are excluded, and also in mice habituated to the treadmill.

(**A**) Same plot as Figure 2E, after removing all periods of detectable whisker or treadmill movements. Visual responsiveness (X-axis) plotted against desynchronization during dilation (Y-axis) for cells from S1, V1, and V1 in FVB mice. Because some data have been excluded, fewer cells show significant individual effects. (**B**)   Overall, cells are still robustly desynchronized during dilation in S1 (7.7±1.8% reduction in 2-10 Hz Hilbert amplitude during dilation, mean ± SEM, $P<.01$) and V1 (15.3±3.4% reduction, $P<.01$, t-test). The effect of dilation was in the same direction for FVB cells (9.8±4.9% reduction), but was no longer significant. (**C**) Pupil diameter increases significantly during running in mice habituated to head restraint on the treadmill for five days for 30 minutes per day (n=113 running epochs in 3 mice; 102±5 μm, mean change ±SEM, $P<.0001$, paired t-test). (**D**) Similar to naïve mice, in habituated mice the amplitude of 2-10 Hz oscillations is reduced during active periods of whisking and running compared to quiet wakefulness (-1.5±.2 mV, $P<.001$; paired t-test; n=10 cells in 3 mice; experiments performed after habituation on the treadmill for 30 minutes per day x 5 days). (**E,F**) There is a strong relationship between pupil dilation/constriction and low-frequency oscillations in habituated mice, similar to naïve mice (2-10 Hz Hilbert amplitude reduced during dilation by 26.5±5.1%, p<.01, t-test).
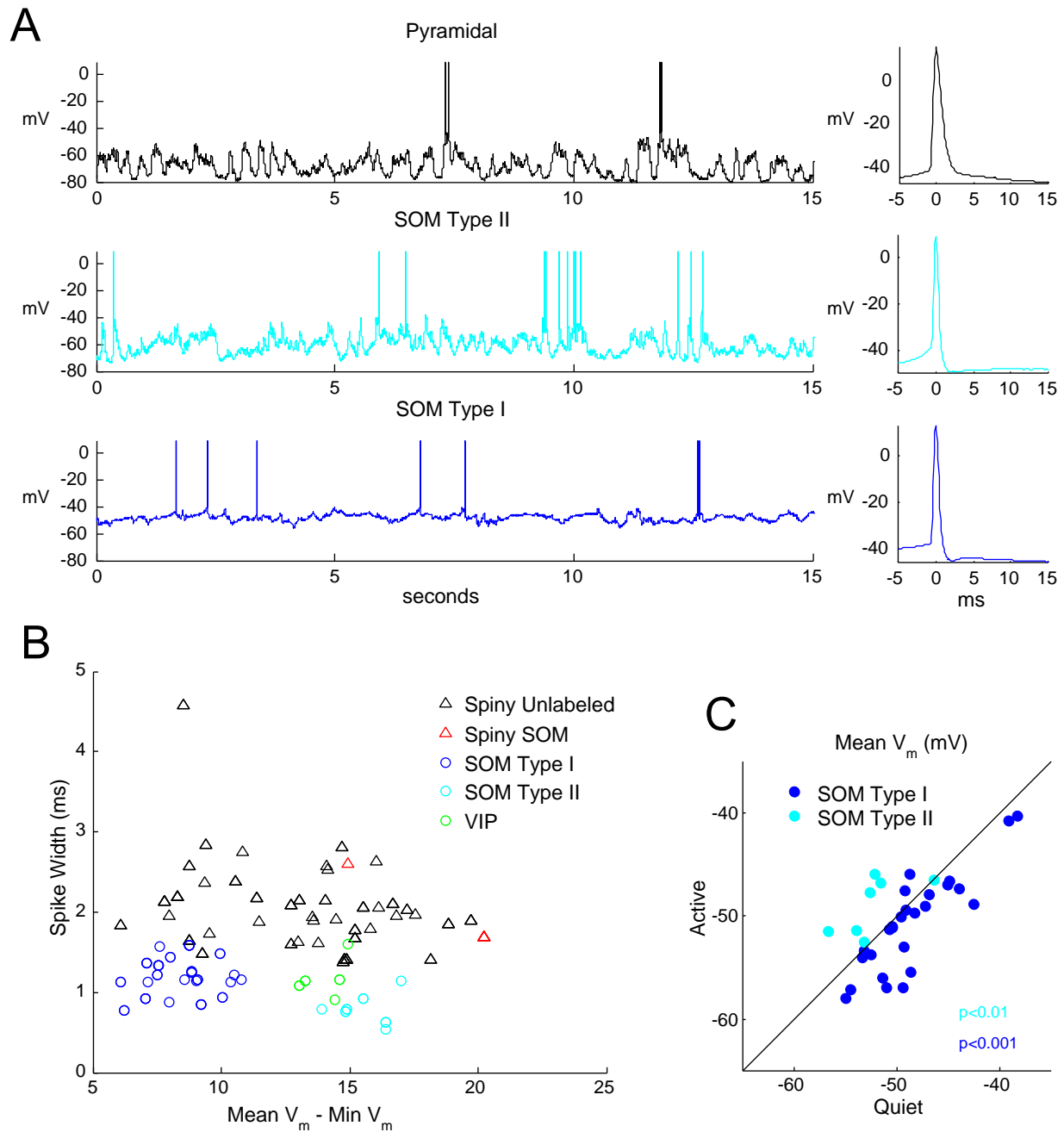
Figure S5, related to Figure 3. Two types of SOM+ labeled cells based on electrophysiological properties have different functional properties.

(**A**) Example traces (left) and average spike waveform (right) for a pyramidal cell (top, black), a SOM+ labeled "Type II" cell (middle, cyan), and a SOM+ labeled "Type I" cell (bottom, blue).

The Type II cell displays large fluctuations in V_m similar to a pyramidal cell, but has a narrow spike waveform. The Type I cell displays comparatively much lower membrane potential variance, and also has a narrow spike waveform. (**B**) Spike width plotted against the difference between the mean and minimum spontaneous V_m for cells of multiple types. Type I (blue) and Type II (cyan) SOM+ cells form two distinct clusters. Pyramidal cells (black) and VIP+ cells (green) are included for reference. Two SOM+ labeled cells with a pyramidal (spiny) morphology likely due to leakiness in the Cre line are indicated in red. (**C**) SOM Type I and Type II cells respond differently during active behavior (running and whisking). Type I cells are inhibited by running (*P<*.001; n=27 cells), while Type II cells are depolarized (*P<*.01; n=7 cells; paired t-test).
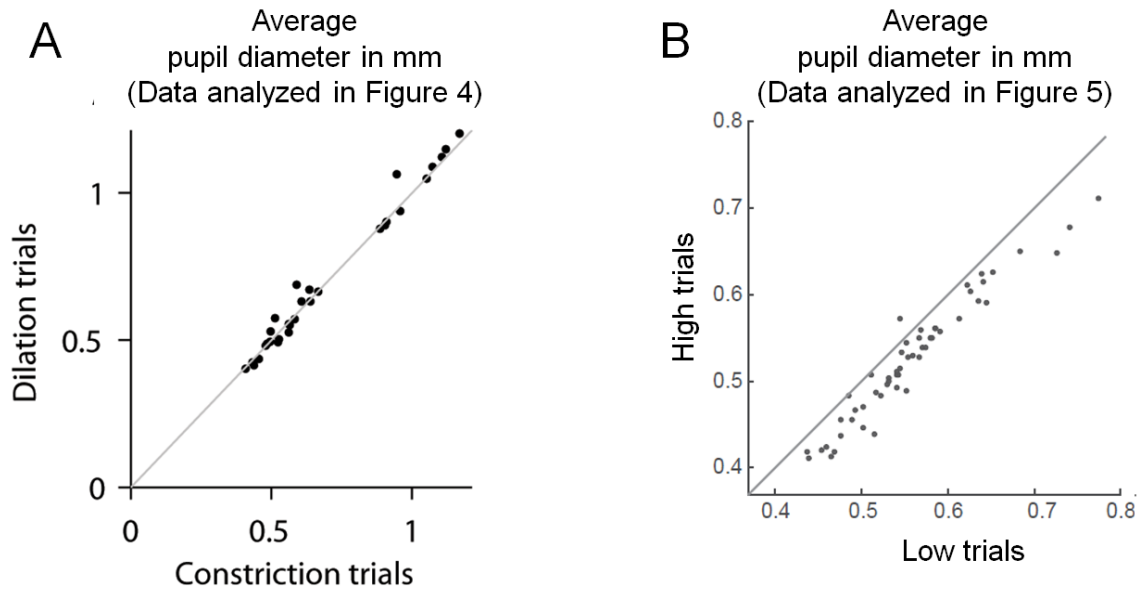
Figure S6, related to Figures 4 and 5. Pupil diameter is not larger during dilating or high trials, when visual responses are enhanced. (**A**) Pupil diameter is not significantly different for dilating trials compared to constricting trials for analysis in Figure 4. Each dot represents an individual imaging site (n=30 sites). (**B**) For analysis in Figure 5, pupil diameter is smaller during High trials (defined by dilation/constriction rate for each site), when visual responses are enhanced. Each dot is average over movie bins for each site (n=53 sites, P<0.001).

Movie S1, related to Figure 1. Pupil fluctuations during quiet and active periods. Fifty seconds of synchronized video from pupil and whisker cameras played at actual speed. Dilating and constricting periods are indicated by a red or blue outline, respectively. The movie begins during a period of quiet wakefulness. In the second half of the recording there are two active periods with locomotion ("RUNNING") and whisking ("WHISKING"); these and similar periods are excluded from all analysis of quiet wakefulness. Smaller detected whisker movements and treadmill movements labeled ("EXCLUDE") are excluded from the analysis in Figure S4, above.

Movie S2, related to Figure 2. V_m transitions between synchronized and desynchronized states during quiet wakefulness. Forty seconds of video of the eye, with the simultaneous filtered 2-10Hz Hilbert amplitude of V_m. Dilations and constrictions are indicated by a blue or red outline, respectively, and red or blue segments of the amplitude trace. The low-frequency amplitude tends to peak during pupil constriction. Black vertical line indicates time of current movie frame in V_m trace.

Supplemental Experimental Procedures

Animals and Surgery

All procedures were carried out in accordance with the ethical guidelines of the National
Institutes of Health and were approved by the Institutional Animal Care and Use Committee
(IACUC) of Baylor College of Medicine. In this study we use data from a total of 51 mice, aged 6
weeks to 6 months. For the patching experiments in Figures 1-3, we used 38 total mice. These
included 34 C57Bl/6 mice (16 males, 22 females). Several of these mice were SST-Cre/Ai9 (n =
16), VIP-Cre/Ai9 (n = 6), or PV-Cre/Ai9 (n = 8) crosses on a C57Bl/6 background, where these
interneuron subtypes were labeled with the fluorescent marker tdTomato. We also used 4
female FVB mice (two 8-week old and two 4-month old mice) for patching experiments. For the
imaging experiments in Figures 4 and 5, we used an additional 13 male C57/Bl6 mice (7 mice for
Figure 5, and 6 mice for Figure 4 including 1 PV-Cre/Ai9 mouse and 1 PV-Cre/Ai27 mouse; a
small number of labeled cells in these recordings were not analyzed differently. Cre lines,
reporters, and FVB mice are all from Jackson Labs as follows:

- SOM-Cre: http://jaxmice.jax.org/strain/013044.html
- VIP-Cre: http://jaxmice.jax.org/strain/010908.html
- PV-Cre: http://jaxmice.jax.org/strain/008069.html
- Ai9 reporter: http://jaxmice.jax.org/strain/007909.html
- Ai27 reporter: http://jaxmice.jax.org/strain/012567.html
- FVB/NJ mice: http://jaxmice.jax.org/strain/001800.html

Anesthesia was induced with 3% isoflurane and maintained with 1.5% to 2% isoflurane during
the surgical procedure. Mice were injected with 5-10 mg/kg ketoprofen subcutaneously at the
start of the surgery. Anesthetized mice were placed in a stereotaxic head holder (Kopf
Instruments) and body temperature was maintained at 37C throughout the surgery using a

homeothermic blanket system (Harvard Instruments). After shaving the scalp, bupivicane (0.05 cc, 0.5%, Marcaine) was applied subcutaneously under the scalp, and Ketoprofen (5–10 mg/kg, s.c.) was given for systemic analgesia. After 10-20 minutes an approximately 1 cm^2 area of skin was removed above the skull and the underlying fascia was scraped and removed. The wound margins were sealed with a thin layer of surgical glue (VetBond, 3M), and a headbar was attached with dental cement (Dentsply Grip Cement). At this point, the mouse was removed from the stereotax and the skull was held stationary on a small platform by means of the newly attached headbar. Using a surgical drill and HP 1/2 burr, a ~3 mm craniotomy was made centered on the area of interest (V1: 2.7mm lateral of the midline, contacting the lambda suture; S1: 3.3mm lateral and 1.5mm posterior of bregma), and the exposed cortex was washed with ACSF (125mM NaCl, 5mM KCl, 10mM Glucose, 10mM HEPES, 2mM CaCl$_2$, 2mM MgSO$_4$). In mice used for calcium imaging, one or two injections of Oregon Green 488 BAPTA-1 AM (OGB-1, Invitrogen; with 2% Pluronic F-127 in DMSO) were made in V1 under two-photon guidance (2-5 μm pipette tip, 40-200 mbar pressure, 0.5-1 μl total volume, targeted to 350 μm below the pia). The cortical window was then sealed with a 3 mm coverslip (Warner Instruments), using VetBond. In mice used for patching, the same 3 mm craniotomy was sealed with a coverslip with a ~500 μm hole that had been previously drilled with a diamond-tipped burr (Coltene/Whaledent). In this case, the hole in the coverslip was positioned to allow access the cortical area of interest with the patch pipette(s).

Behavioral recordings

After surgery, the mouse's head was restrained above the spherical or cylindrical treadmill and the mouse was allowed to recover on a heating pad placed on top of the treadmill. Once awake, the mouse was given 30-60 minutes to fully recover from the effects of anesthesia and acclimate to head fixation. In some experiments the animals were habituated to the recording apparatus by head-restraining them on the treadmill for thirty minutes per day for five consecutive days before performing the craniotomy and recording. The treadmill rotated on a single axis so that treadmill movement was restricted to the rostro-caudal axis of the mouse. In some cases, movements were detected with an optical mouse and digitized at 200 Hz, while in others treadmill motion was measured using a rotary optical encoder with a resolution of 8000 counts/revolution. Running periods were defined as periods of one second or more with treadmill speeds above 1 cm/sec. Intervening periods of less than one second between running epochs were also included as running.

The mean increase in pupil size during running in Figures 1D and S2C was calculated after excluding running periods that occurred less than 10 seconds after a previous running period, in order to avoid cases where the pupil was already dilated by running. With this restriction, we found that 92% of running epochs in figure 1D were associated with an overall increase in pupil size. For about two-thirds of these epochs (67%), the increase in pupil size was greater than three times the standard deviation of diameter during the pre-running baseline (taken as the 10 seconds preceding run onset).

For C57Bl/6 mice, the eye was illuminated with a 680 nm or greater wavelength LED array and pupil position and size were recorded at 1280×1024 at 10 Hz on setup A (DCC1545M

camera, Thorlabs, with TML-HP 1x Telecentric lens, Edmund Optics) , and at 60 Hz on setup B (CR-GM00-H6400, Teledyne Dalsa). Because of the lack of pigmentation, red light did not provide sufficient contrast to illuminate the pupils of retinally-blind FVB mice, and oblique illumination with 490 nm light was used instead. The eye was not illuminated at all while testing for visual responsiveness in these mice. Whisking was recorded at 640×480 or 320×240 at 250 Hz with a separate camera (CR-GM00-H6400, Teledyne Dalsa) on setup A, or with the same camera used to record the eye on setup B. All behavioral data was acquired with custom software written in LabView (National Instruments).

Post-hoc pupil segmentation was performed with custom software written in MATLAB (Mathworks) and manually supervised. Reflection of the light source and visual stimulus on the eye were both masked from each frame of the image, which was smoothed using a 2D Gaussian kernel (σ=5-10 pixels) and thresholded to isolate the darker pixels in the pupil. A circle was least-squares fit to the points along the edge of this region (Image Processing Toolbox, MATLAB; fitcircle, Richard Brown, Mathworks File Exchange). The detection threshold, smoothing widths, visual stimulus and specular reflection rejection were adjusted manually by visual inspection of the detection fit of every 10th frame (setup A) or every 20th frame (setup B).

Whisking was detected by extracting the optic flow from a manually-selected ROI of whisking movies (OpticalFlow Object, Computer Vision System Toolbox, MATLAB). Whisking and noise thresholds were set manually based on visual inspection of the optic flow trace and raw video. This analysis allowed sensitive detection of even small whisker movements, but did not allow full reconstruction of the whisker trajectory. We did not have high-speed video for

16

some of the recordings with patch data and all of the recordings with calcium imaging on Setup A (grating stimulus). In these cases we used movements of the face and whisker pad captured by the eye imaging camera to identify whisking periods. Comparing these data to the high-speed video, we found that this measurement captured more than 85% of the whisking periods where high speed video was available, as well as many of the smaller subthreshold movements associated with postural adjustments on the treadmill. We thus used whisker pad movement as a proxy for direct visualization of the whisker in the recordings without high-speed video. Whisking periods were defined as periods of suprathreshold activity of one second or more, and intervening periods of less than one second between whisking epochs were also included as whisking.

Visual stimuli

Grating stimuli were presented on a 7" LCD monitor (Lilliput 665GL-70NP/HO/Y monitor; 60 Hz scan rate; setup A) positioned 10 cm away from the eye, covering approximately 88° (azimuth) by 72° (elevation) of the contralateral visual field. Natural movie stimuli were presented on a 30" LCD monitor (U3011t, Dell, 60Hz refresh rate; setup B) positioned ~30 cm away from the animal's eye, covering 94° (azimuth) by 67° (elevation) of the contralateral visual field. For the grating stimulus, full-field square wave gratings (spatial frequency 0.04 Hz, temporal frequency 2 Hz) were presented at eight orientations (100 blocks containing all orientations in random order). Gratings were presented for 500 ms and separated by a 1-second luminance-matched gray background. Stimulus presentation routines were written in MATLAB using the Psychophysics Toolbox (Brainard, 1997; Pelli, 1997). A photodiode attached to the

screen allowed exact time-stamping of each frame of the stimulus presentation. Natural movies were acquired as previously described (Froudarakis et al., 2014). Briefly, recordings were made from a head-mounted webcam while the mouse ran freely in an enriched and spacious (~0.5 m²) environment. We used 10 s clips of these movies, which contained periods of locomotion, looking around and resting.

Calcium imaging

Two-photon imaging of OGB fluorescence was performed on modified Sutter microscopes. Imaging on setup A was performed with a fast resonant scanning system (ThorLabs, typically at 30 Hz). Imaging on setup B was performed with a galvo-galvo scanning system (Sutter Instruments, typically at 12 Hz). Excitation on both setups was via a Ti-Sapphire laser (Chameleon Vision, Coherent) tuned to either 800 nm or 1000 nm and either a 20× (1.0 NA, Olympus) or 25× (1.1 NA, Nikon) objective. Power out of the objective was controlled by calibrated rotations of a half-wave attenuator and depended on the magnification of the scan but was always kept below 50 mW.

Avoiding neuropil contamination of calcium signals during functional imaging is important and often underappreciated. Using high NA objectives to restrict the size of the point-spread function is critical. Typical empirical PSFs measured with our objectives were approximately 300 nm (Nikon) or 400 nm (Olympus) in both X and Y, and approximately 2 μm in Z (both objectives; full width at half-height). Characterizing and reducing movement of the prep is also important. Motion in the X-Y plane was corrected with post-hoc raster correction and sub-pixel motion correction prior to extracting calcium traces. We could not correct

movement in the Z-plane, but with our chronic window preparations typically motion in Z was very small. For about half the recordings used in Figure 4, we estimated the magnitude of Z motion by taking a high-resolution (500 nm step) Z-stack following each scan and registering each frame in the recording to this stack. Mean Z motion was slightly higher during running than quiet wakefulness, measured as the absolute displacement from the mean Z-position during each scan (running: mean 1.2 μm, s.d. 0.6μm; quiet: mean 0.88 μm, s.d. 0.46 μm).

Whole-cell patching

Patch pipettes were pulled from borosilicate glass (1.5 mm OD × 0.86 mm ID, Sutter Instruments) to an impedance of 6-10 MΩ. Pipettes were filled with standard internal solution (Jiang et al., 2013) (125mm Potassium Gluconate, 10mM HEPES, 4mM Mg-ATP, 0.3mM Na-GTP, 10mM Na_2-Phosphocreatine, 13 mM biocytin, pH 7.25, osmolarity normalized to extracellular solution) and Alexa 488 or 598 was added (50 μM) to allow visualization of the pipette and extracellular space. A manometer (Fisher Scientific 06-664-19) and custom-built pressure manifold allowed fast switching between high pressures while entering the bath and penetrating the dura (~150 mbar), and low pressures (~20-50 mbar) while advancing the pipette through the cortex under two-photon guidance, which helped to reduce the overall volume of intracellular solution ejected from the pipette. Bias currents were zeroed once the pipette was placed in the bath. Gigaseals were allowed to stabilize for 3-5 minutes before break-in. Compensating for tissue distortion by retracting the pipette ~10 μm during this time resulted in improved access and more stable recordings. V_m was not adjusted for the liquid junction potential.

Preprocessing of calcium imaging data

For data from the galvanometric scanning system (setup B), we performed motion compensation in the horizontal plane, and cell detection was automated by detecting circular regions based on minimum diameter, cell contrast, edge sharpness and maximum number of cells per site, and the results were manually supervised and corrected if necessary. For resonant scanning data (setup A) cell detection was performed entirely manually. The data processing chain for this and subsequent analysis relied on the DataJoint library for MATLAB (http://datajoint.github.com/datajoint-matlab/). Calcium traces averaged from all pixels in segmented cells were normalized to ΔF/F, down-sampled to 10-20 Hz and then filtered by using a nonnegative deconvolution algorithm (Vogelstein et al., 2010) to infer instantaneous firing rates. The parameters of the algorithm were optimized to yield optimal reconstruction (lambda = 0.3) as previously described (Cotton et al., 2013; Froudarakis et al., 2014).

Analysis of patching data

After removing detected spikes, the amplitude of low-frequency oscillations was measured by filtering raw V_m from 2-10 Hz, taking the Hilbert amplitude of this oscillation, and filtering the resulting trace between 0.1 and 1 Hz (pupil phase plots in Figure 2D,3E), or low-pass filtering below 1Hz (all other figures). For registration to a standard dilation/constriction cycle in the phase plots, whisking, running and saccades were excluded from analysis, and the filtered V_m and Hilbert amplitude at each time point were binned by the Hilbert phase of the filtered (0.1 to 1 Hz) pupil trace (64 bins from $-\pi$ to π). In the phase plot analysis, the data were restricted to the same periods of pupil dilation and constriction used in Figure 2E-H (duration greater than

one second, with absolute dilation or constriction rates greater than 10 μm/s) Means of binned

data in Figure 2D, Figure 3E, and Figure S3 were smoothed by averaging with adjacent bins.

Analysis of responses to moving gratings (Figure 4)

Orientation tuning was computed by linear regression of the deconvolved calcium trace to the

stimulus conditions (drifting directions). Mean tuning curves in Figure 4C,D are smoothed with

the Hamming filter with 40-degree support. In figure 4C, we restricted the analysis to

recordings with at least one minute of total running time (n=516 cells in 19 sites), in order to

correctly estimate the tuning of cells during both conditions. The reliability of responses across

visual stimuli was calculated as the fraction of variance explained by the average response

binned in 150 ms bins limited to stimulus conditions with at least 16 repeats in each state.

Significance was calculated using the number of sites as the degrees of freedom rather than the

number of cells in order to avoid the potential confounding effects of correlations between cells.

The preferred direction was found by fitting the two-peaked von Mises function to all data

irrespective of condition. OSI was then calculated for each cell under each condition as the

difference between the mean response to this preferred direction and the mean response to the

orthogonal direction, normalized by their average. Trials with any overlap with running or

whisking periods were treated as "active," and these trials were excluded from further analysis

in Figure 4. Trials with saccades or blinks were also excluded from analysis. Trials were

classified as "constricting" or "dilating" based on the difference in pupil size from the start to

the end of the trial, and trials with absolute dilation or constriction rates less than 10 μm/s were

excluded. Noise correlations were calculated as correlations between residual signals after

subtracting the mean stimulus responses binned in 150 ms intervals and normalized by the standard deviation of responses in each bin. Signal correlations were calculated as correlations between mean stimulus responses binned in 150 ms intervals.

Analysis of responses to natural movies (Figure 5)

To account for changes in pupil diameter due to luminance changes in the natural movies, we first binned the movies, neural responses, and the rate of change of the pupil diameter in 150 ms bins. Each bin contained a few frames of the movie (here we refer to these bins as "scenes"). For each scene, we sorted all repetitions of that scene (trials) by the rate of change of the pupil diameter, and for each cell we compared the neural responses in the 25% of trials with the lowest rates of pupil change ("low") to the neural responses to the same scene in the 25% of trials with the highest rates of pupil change ("high"). Signal correlations were calculated as the mean Pearson correlation between average response traces across all pairs of cells in each imaging site. To compute noise correlations we first computed the z-scores across trials for each scene. Noise correlations were calculated as the Pearson correlation between the computed z-scores averaged across each imaging site. The reliability of each cell was defined as the variance of the average response across movie repetitions divided by the total variance over the entire recording. To measure discriminability, we used an optimal linear classifier assuming isotropic covariance matrices and leave-one-out cross-validation to estimate the decoding error between the neural representations of pairs of scenes. Each scene was represented as an N-dimensional vector of neural activity for each trial. We converted the decoding error to discriminability, the mutual information (measured in bits) between the true class label c and its estimate $\hat{c}$ by

computing

$$MI(c, \hat{c}) = \sum_{i \in 1,2} \sum_{j \in 1,2} p_{ij} log_2 \frac{p_{ij}}{p_{i \cdot} p_{\cdot j}},$$

where p_{ij} is the probability of observing true class i and predicted class j, and $p_{i \cdot}$ and $p_{\cdot j}$ denote the respective marginal probabilities.

To compute the change in the mean firing rate for different scenes (Figure 5D,E), we sorted the scenes by response magnitude of each cell (not taking pupil dilation/constriction into account), ordering them from least-preferred (smallest response) to most-preferred (largest response). We then grouped the sorted scenes into quartiles: 0%-25% (least-preferred scenes), 25%-50%, 50-75%, and 75%-100% (most-preferred scenes) and examined the difference in single-cell responses between the high and low conditions for each of these quartiles. Percent change was defined as (response_high - response_low) / response_high. Error bars were computed as 95% bootstrap confidence intervals with 5000 resamples. For this analysis we only included the cells that were reliably driven by the stimulus (>30% of the response variance explained in either the low or high condition; n=467/1249 neurons).

Supplemental References

Brainard, D.H. (1997). The Psychophysics Toolbox. Spatial vision *10*, 433-436.

Cotton, R.J., Froudarakis, E., Storer, P., Saggau, P., and Tolias, A.S. (2013). Three-dimensional mapping of microcircuit correlation structure. Front Neural Circuits *7*, 151.

Froudarakis, E., Berens, P., Ecker, A.S., Cotton, R.J., Sinz, F.H., Yatsenko, D., Saggau, P., Bethge, M., and Tolias, A.S. (2014). Population code in mouse V1 facilitates readout of natural scenes through increased sparseness. Nat Neurosci *17*, 851-857.

Jiang, X., Wang, G., Lee, A.J., Stornetta, R.L., and Zhu, J.J. (2013). The organization of two new cortical interneuronal circuits. Nat Neurosci *16*, 210-218.

Pelli, D.G. (1997). The VideoToolbox software for visual psychophysics: transforming numbers into movies. Spatial vision *10*, 437-442.

Vogelstein, J.T., Packer, A.M., Machado, T.A., Sippy, T., Babadi, B., Yuste, R., and Paninski, L. (2010). Fast nonnegative deconvolution for spike train inference from population calcium imaging. J Neurophysiol *104*, 3691-3704.